Plasmon Dispersion in Coaxial Waveguides from Single-Cavity Optical Transmission Measurements

René de Waele,*,† Stanley P. Burgos,‡ Albert Polman,† and Harry A. Atwater‡

*Center for Nanophotonics, FOM Institute for Atomic and Molecular Physics,
Science Park 113, 1098 XG Amsterdam, The Netherlands, and California Institute of
Technology, 1200 East California Boulevard, Pasadena, California 91125*

ABSTRACT

We determine the plasmon dispersion relation in coaxial waveguides composed of a circular channel separating a metallic core and cladding. Optical transmission measurements are performed on isolated coaxial nanoapertures fabricated on a Ag film using focused ion-beam lithography. The dispersion depends strongly on the dielectric material and layer thickness. Our experimental results agree well with an analytical model for plasmon dispersion in coaxial waveguides. We observe large phase shifts at reflection from the end facets of the coaxial cavity, which strongly affect the waveguide resonances and can be tuned by changing the coax geometry, composition, and surrounding dielectric index, enabling coaxial cavities with ultrasmall mode volumes.

In only a few years time the rapidly growing field of plasmonics has generated a large array of new nanophotonic concepts and applications. The ability of metal nanostructures to localize light to subwavelength volumes[1−3] has provided opportunities for, e.g., sensing applications[4] and nanoscale optical lithography.[5,6] Plasmonics also provides a way to finely tailor the dispersion relation of light, giving the ability to shrink the wavelength of light down to only a few tens of nanometers at optical frequencies,[7] or create materials with negative index of refraction.[8] Possible applications where precise control of the optical dispersion is essential range from true-nanoscale optical components for integration on semiconductor chips to lenses for subwavelength imaging[8,9] and invisibility cloaks.[10,11]

Recently, coaxial plasmon waveguides with a circular dielectric channel separating a metallic core and cladding, have received a great deal of attention in connection to observed enhanced transmission from two-dimensional arrays of coaxial nanoapertures at infrared wavelengths.[12−14] The transmission enhancements have been ascribed to standing optical waves along the axis of the coaxial apertures.[15−17] Past studies have been limited to short (<200 nm) coaxial channels, allowing observation only of the lowest order resonances.[12−14] Furthermore, optical transmission has only been measured for arrays of coaxial waveguides, making it hard to separate transmission enhancements owing to channel

resonances from enhancements related to collective resonances of the array.[12−14,18] To investigate the optical resonances of coaxial waveguides in detail, measurements on single coaxial nanostructures are necessary. Furthermore, a systematic study is needed of the phase shifts upon reflection from the waveguide ends, as they strongly affect the resonances of a short waveguide.

Here, we report optical transmission measurements of isolated coaxial plasmon waveguides in Ag with systematically varied lengths in the range 265−485 nm. By variation of the channel length, the dispersion relation for these structures was determined for the first time. The experimental results agree well with an analytical model for plasmon dispersion in coaxial waveguides. We observe a significant enhancement of the wave vector of light when coupled to coaxial waveguides from free-space, even at frequencies well below the surface plasmon resonance. It is found that the phase shift upon reflection off the waveguide ends can be tuned by changing the waveguide geometry. We anticipate that the combination of strong optical confinement and relatively low propagation loss make coaxial waveguides very promising as nanoscale optical components.

The plasmon dispersion in coaxial waveguides was determined from transmission measurements of isolated coaxial channels prepared using focused ion beam (FIB) milling on films of Ag. Ag was deposited by thermal evaporation on quartz substrates. The Ag thickness was varied between 265 and 485 nm in 20 nm increments using

* Corresponding author, waele@amolf.nl.
† Center for Nanophotonics, FOM Institute for Atomic and Molecular Physics.
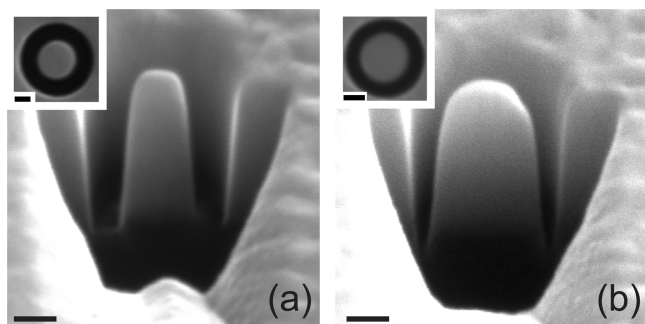‡ California Institute of Technology.

Figure 1. SEM images of the cross-sectional profile of coaxial plasmon waveguides with lengths of 485 nm, dielectric channel widths of ∼100 nm (a) and ∼50 nm (b), and outer radii of ∼175 nm. The insets show top-view SEM images of the waveguides before cross sectioning. Scale bars are 100 nm.

a shutter. We fabricated coaxial waveguides by FIB milling 20−100 nm wide circular channels through the Ag layer. Figure 1 shows scanning electron microscope (SEM) images of 485 nm long coaxial channels with an outer radius of ∼175 nm and channel widths of ∼100 nm (a) and ∼50 nm (b). The main panels in Figure 1 were taken at a 55° angle with respect to the sample normal after a cross section was made using FIB milling. The images display a small degree of tapering of the channels (∼7° taper angle), which is mainly caused by redeposition of Ag in the waveguide during FIB milling, an effect that becomes more pronounced deeper in the Ag layer. The insets in Figure 1 are top-view SEM images of the coaxial channels that show excellent uniformity of the channel radii and width. Coaxial channels were separated by 50 μm to avoid coupling between waveguides.

To investigate the influence of channel length and width on the optical response of coaxial waveguides, we performed optical transmission measurements. Radiation from a super-continuum white light source was focused onto individual coax structures using a 0.95 NA objective. The transmitted light was collected by a 0.7 NA objective and directed into a spectrometer equipped with CCD detector to measure optical spectra. For reference, we measured transmission spectra of 10 × 10 μm open squares in which the Ag layer had been completely removed by FIB milling. Figure 2 shows transmission spectra of a 100 nm wide, 485 nm long coax channel (I) and of a reference area close to the waveguide (I_0). The transmittance spectrum ($T = I/I_0$) is obtained by normalizing the waveguide transmission to the reference spectrum and is also shown in the figure. Three distinct maxima can be resolved in the transmittance spectrum, at ∼450, ∼600, and >820 nm, which we attribute to Fabry−Perot cavity resonances of the coaxial waveguide. To corroborate this hypothesis, we have measured the transmittance of a series of coaxial waveguides of equal channel width but varying channel lengths.

Figure 3 shows transmittance spectra of 100 nm wide coaxial channels with length decreasing from 485 nm (same data as in Figure 2) to 265 nm in 20 nm increments. Several features are observed. First, the resonance at 600 nm for the longest waveguide gradually blue shifts to 450 nm for the shortest waveguide. Also, the resonance at 450 nm, observed
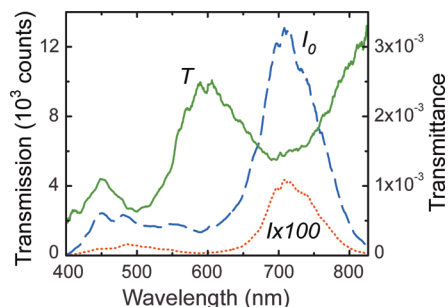

Figure 2. Transmission measurement (red dotted spectrum, I multiplied by 100) of a coaxial waveguide with ∼100 nm wide dielectric channel and length of 485 nm (see Figure 1b) and a reference spectrum (blue dashed line, I_0). The transmittance defined as the waveguide transmission spectrum divided by the reference spectrum is depicted by the green curve (green drawn line, T).
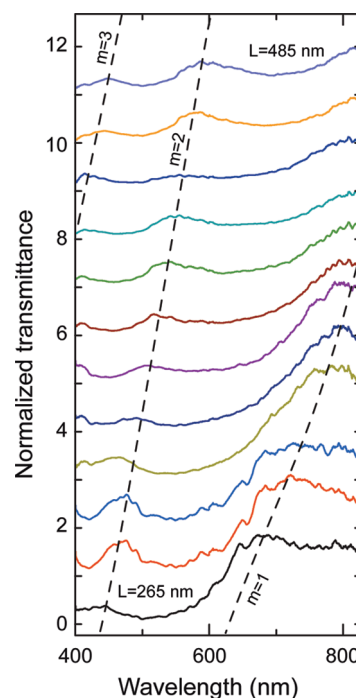

Figure 3. Transmittance spectra of coaxial waveguides with varying lengths. The outer radius and channel width were ∼175 and ∼100 nm, respectively, while the waveguide length was decreased from 485 nm (top curve) to 265 nm (bottom curve) in increments of 20 nm. Data are shifted vertically for clarity. The black dashed lines are guides for the eye and connect the resonance peaks ($m = 1-3$).

for the largest channel length, blue shifts to a wavelength below 400 nm for waveguides shorter than 400 nm. The broad peak in the long-wavelength range of the spectra also blue shifts as the length of the cavity is decreased, showing a main peak at a wavelength of 650 nm for the shortest waveguides. Furthermore, the lowest-order resonances observed in the three shortest waveguides appear to be much broader than other resonances. This is possibly the result of a longer-wavelength resonance that arises when all propagating modes in the resonator are in cutoff.[18]

Fabry−Pérot resonances result from interference between forward and backward propagating plasmon waves in the cavity. On resonance, the condition

$$|2Lk_{SPP}(\omega) + \Delta\phi_1 + \Delta\phi_2| = 2\pi m \qquad (1)$$

must be fulfilled, with L the length of the waveguide, $k_{SPP}(\omega)$ the wave vector of the plasmon at frequency ω, $\Delta\phi_{1,2}$ the phase shifts as a result of plasmon reflection at either end of the waveguide, and m the mode number.

Before we can determine the plasmon dispersion in coaxial waveguides, it is necessary to assign mode numbers to the measured Fabry−Pérot resonances. With this in mind, we performed exact calculations of $k_{SPP}(\omega)$ by solving Maxwell's equations for a cylindrical structure of infinite length.[15,16,19−21] The azimuthal dependence of the electric and magnetic fields in the waveguide is described by the harmonic function $e^{in\psi}$ of order n. Note, that we expect to only excite modes of odd azimuthal order in the experiment as the incident electric field has even parity about the center of the waveguide aperture. The radial dependence of the fields in all three domains (Ag−dielectric−Ag) is described by solutions to the second-order Bessel differential equation. We apply a Bessel function of the first kind, J_n, to the Ag core and a Hankel function of the first kind, $H_n^{(1)}$, to the Ag cladding. Inside the dielectric channel the radial field dependence is described by a linear combination of Bessel and Hankel functions of the first kind. On each domain boundary we formulate four continuity conditions for the tangential components of the electric and magnetic fields. The optical eigenmodes of the coaxial waveguide are found when the determinant of the resulting homogeneous system of eight equations with eight unknown coefficients vanishes.

In this way dispersion relations were determined for waveguides of any chosen channel width. To account for the tapered profile of the resonators in the experiment, we calculated the effective dispersion relation by index-averaging $k_{SPP}(\omega)$ over a series of dispersion curves corresponding to the varying lateral dimensions of the waveguide determined from SEM images (Figure 1). By inserting this index-averaged dispersion into eq 1, we obtain the resonance frequency as function of cavity length and mode number m. We compared these results to experimental values of the resonance frequency, obtained by fitting the transmittance spectra with Lorentzian line shapes, as a function of waveguide length. This comparison makes it possible to assign mode numbers to the measured resonances and construct the plasmon dispersion relation for the coaxial waveguides. In the following first analysis we assume that the plasmon phase shift upon reflection at the cavity ends, which will be discussed further on, is zero.

Figure 4a shows the dispersion data for coaxial channels with an average outer diameter of ∼175 nm and ∼50 nm wide air channel (see Figure 1b) along with the calculated dispersion curve for azimuthal order $n = 1$, taking into account the tapering in the structures as determined from SEM data (Figure 1). Good agreement between experiment and calculations is observed. Different symbols indicate measured resonances characterized by mode numbers, $m = 1$ and 2. Dispersion in air and at a Ag/air interface are plotted for reference. The figure shows up to ∼60% larger wave vectors in coaxial waveguides compared to free space. At
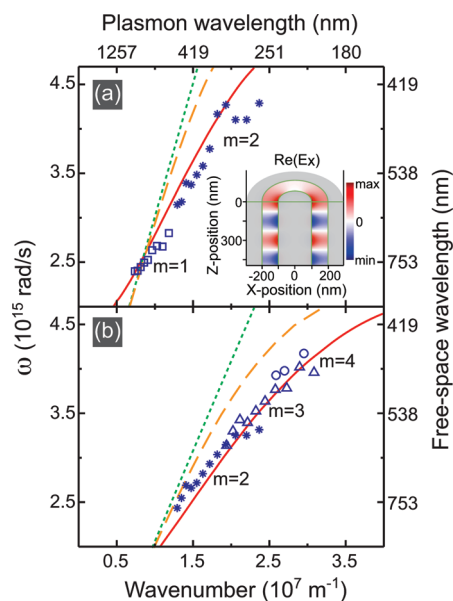

Figure 4. Measured dispersion data and calculated index-averaged dispersion relations (red drawn lines) for coaxial plasmon waveguides with (a) ∼50 nm wide air channel and (b) ∼50 nm wide spin-on-glass (SOG) filled channel. Light lines for air (a) and SOG (b) are also shown (dotted green lines), along with the plasmon dispersion (dashed orange curves) at a flat Ag/air interface (a) and Ag/SOG interface (b). Symbols in the figure correspond to different Fabry−Pérot mode numbers, m, where □ = 1, * = 2, △ = 3, and ○ = 4. The inset in (a) shows the calculated electric field distribution of the mode of azimuthal order $n = 1$, in an SOG-filled coaxial waveguide with outer radius of 200 nm and channel width of 100 nm at $\omega = 3.5 \times 10^{15}$ rad/s.

lower frequencies ($\omega < 2.5 \times 10^{15}$ rad/s), as the mode approaches cutoff, the calculated dispersion relation flattens slightly and crosses the air light line, in agreement with experimental data in that frequency range. This behavior is not observed in studies of cylindrical metal waveguides when the excited plasmon mode has azimuthal symmetry ($n = 0$),[22,23] as that mode does not experience cutoff.

To further increase the dispersion, we infilled the coaxial nanostructures by spin-coating the sample with a ∼200 nm thick layer of spin-on-glass (SOG, $n = 1.46$). SEM of FIB-milled cross sections confirmed that SOG infilled the structures entirely. Figure 4b shows the dispersion data for infilled coaxial waveguides of the same dimensions as in (a). In this case resonances with mode numbers $m = 2−4$ were observed. We further note a shift of the dispersion data to higher wavenumbers compared to the air case of Figure 4a, as well as a clear increase in the curvature of the dispersion relation. In this case we observe up to ∼2.2 times larger wave vectors in coaxial waveguides compared to free space. Figure 4b also shows the calculated plasmon dispersion (red drawn curve).

Thus far we have demonstrated cases where the calculated dispersion relations match the experimental data quite well. Figure 5a compares the dispersion data (assuming zero phase change on reflection) and calculated dispersion relation (red drawn curve) for air-filled waveguides with a dielectric channel width of ∼100 nm. Although the data follow the same general trend as the calculated curve, the two show a
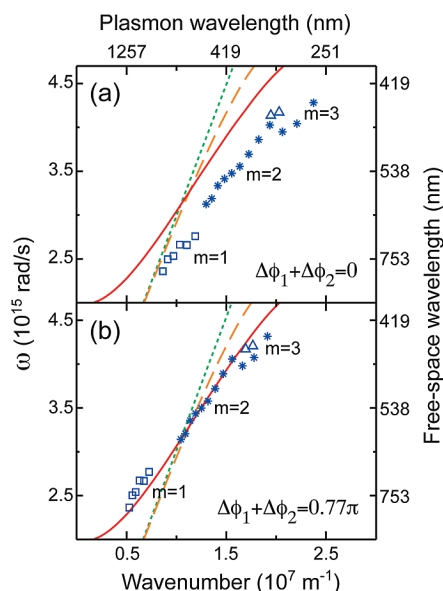
Figure 5. Measured dispersion data and calculated index-averaged dispersion relations (red drawn lines) for coaxial plasmon waveguides with a 100 nm wide air channel. In (a) the dispersion data are plotted, assuming a zero net phase shift as result of reflections at the end facets of the cavity. In (b) the data are plotted for an overall reflection phase shift of 0.77π which was determined using simulations. Light lines for air are also shown (dotted green lines), along with the plasmon dispersion (dashed orange curves) at a flat Ag/air interface. Symbols in the figure correspond to different Fabry−Pérot mode numbers, m, where $\square = 1$, $* = 2$, and $\triangle = 3$.

clear offset in wavenumber with respect to each other. In the final part of this Letter we will show that the observed discrepancy between the data and theory results from a net phase shift ($\Delta\phi_1 + \Delta\phi_2$) that the plasmons gain when they reflect off the cavity ends, which can be tuned by changing the cavity geometry.

As eq 1 shows, a nonzero net phase shift causes the resonance wavelengths to shift. To study the phase shift, we have performed finite difference time domain (FDTD) simulations to obtain the field profile in structures similar to those used in the experiment. In the simulations we used a broad band optical pulse with Gaussian beam profile to excite the structures. By applying a discrete Fourier transform of the time-dependent fields, we obtain the spatial field intensity profiles at any given optical frequency. In Figure 6 we show the simulation results for an air-filled coaxial waveguide of the same dimensions as the structure shown in Figure 1a excited at an angular frequency of 4.2×10^{15} rad/s (free-space wavelength of 450 nm). Figure 6a shows the steady-state intensity distribution in the plane of polarization for the electric field component that is parallel to the polarization direction of the incident light. As in the experiment the waveguide is excited at the air-side (left-side in the figure).

In the steady state, the field profile in the cavity is a superposition of plasmon waves propagating in forward and backward direction after any number of reflections at the input or distal end of the cavity. The analytical expression of the resulting electric field in the cavity as a function of
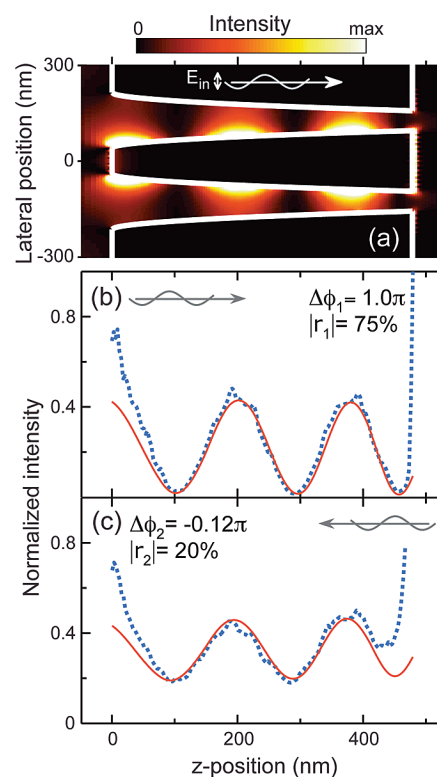

Figure 6. Steady-state simulation results of the electric field intensity profile inside a 485 nm long coaxial cavity with an air-filled $\sim$100 nm wide dielectric channel excited at an angular frequency of 4.2×10^{15} rad/s (free-space wavelength of 450 nm). (a) Electric field intensity distribution inside the coaxial cavity for light incident from the left. (b, c) Intensity as a function of position integrated along the lateral direction (dotted lines) for light incident from the left (b) and right (c). The red drawn curves are fits of the intensity profile that were used to find the reflectance and reflection phase shifts at the distal end facets. The reflection phase shift is 1.0π at the substrate side and -0.12π at the air side of the cavity, while the values for the reflectance are 75% and 20%, respectively.

position in the direction parallel to the waveguide axis, is given by

$$E(z) \propto \mathrm{e}^{ikz} + |r_1|\mathrm{e}^{i(k(L-z)+\langle k\rangle L+\Delta\phi_1)} \qquad (2)$$

where k is the plasmon wave vector (which depends on z as a result of waveguide tapering), $\langle k\rangle$ is the index-averaged wave vector, and $|r_1|$ and $\Delta\phi_1$ are the reflectance and reflection phase shift at the distal end of the cavity, respectively. Note, that the field profile inside the cavity is not affected by the reflectivity of the input end of the waveguide. In fact, the field profile is simply proportional to the original plasmon wave and the plasmon wave after one reflection, added together.

Figure 6b plots the intensity distribution in the cavity as a function of position along the waveguide axis (blue dotted curve), obtained by vertically summing the intensity values in Figure 6a. To obtain the phase shift at the distal end of the waveguide (right end in Figure 6a), we fit the intensity distribution with $|E(z)|^2$ (eq 2). As the plasmon wave vector is calculated analytically, the only fit parameters, besides an

amplitude constant, are $\Delta\phi_1$ and $|r_1|$. The result of the fit is plotted in Figure 6b (red drawn curve). From the fit it follows that the phase shift as result of the reflection at the substrate end of the waveguide is close to π. The visibility of the oscillation depends on the reflectance $|r_1|$ at the distal cavity end. On the basis of the fit we find that the reflectance of the substrate-side end facet is equal to 75%.

To obtain the reflection phase shift at the input end facet, $\Delta\phi_2$, the intensity distribution in the waveguide was simulated for light impinging on the nanostructure from the substrate side of the cavity. We show the result of this simulation in Figure 6c. Owing to a lower reflectance of the air-side end facet of 20%, the visibility of the intensity distribution is smaller. Furthermore we find that the phase shift upon reflection at the air-side cavity end is close to zero. Using the reflectance values as determined from the fits and the calculated waveguide losses, we obtain a cavity quality factor of only ~4, which explains the broad spectral width of resonances in measured spectra. We note however, that the cavity losses are almost entirely due to the rather poorly reflecting end facets of the cavity. By improving the end face reflectivity, it should be possible to attain quality factors of more than 80. Furthermore, on the basis of comparisons with simulations of untapered waveguides, it is important to note that waveguide tapering does not significantly affect the end facet reflectance and, as a result, does not add to the resonance line width. However, tapering does result in a larger dielectric channel width at the input side of the cavity, which, as shown, may give rise to lower end facet reflectance, resulting in a reduction of the quality factor of the cavity.

The analysis in Figure 6 was done at a frequency of 4.2×10^{15} rad/s (free-space wavelength of 450 nm). At lower frequencies, we find that the overall phase shift tends to decrease (data not shown). The average net phase shift we find for frequencies within the experimental bandwidth equals ~0.77π. In Figure 5b we plot the dispersion relation taking into account this average phase shift and observe a close agreement between theory and experiment. Note, that in our analysis of waveguides with a ~50 nm wide dielectric channel (Figure 4) or waveguides filled with SOG, best agreement between experiment and theory was found for phase shifts close to zero, demonstrating that the phase shifts on reflection can be tuned by changing the geometry.

To further investigate the tunability of the reflection coefficients of the coaxial end facets, we simulate the response of waveguides as we vary the refractive index of the dielectric channel and surrounding medium. The simulations are performed using untapered waveguides of 485 nm length and 175 nm outer radius, that are composed of a 75 nm wide dielectric channel separating a Ag core and cladding.

Figure 7 shows the reflectance $|r_1|$ and reflection phase $\Delta\phi_1$ obtained by fitting the longitudinal field intensity profile using eq 2 for a waveguide with Ag core and cladding and dielectric channel at $\lambda_0 = 800$ nm. In Figure 7a the refractive index of the dielectric channel is kept fixed at $n_{in} = 1.5$ while the refractive index of the surrounding medium is varied from
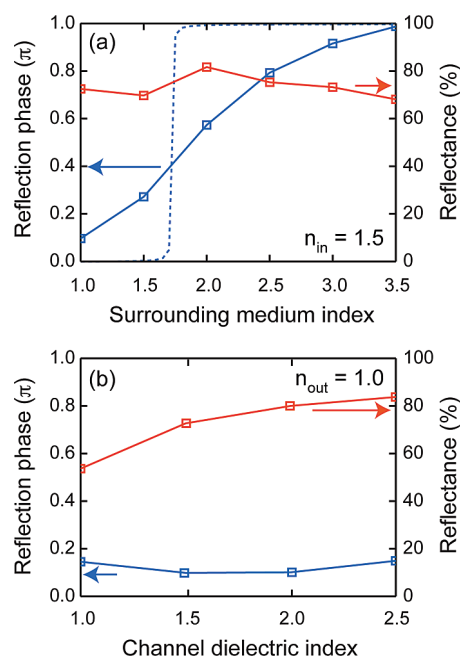

Figure 7. Reflection phase ($\Delta\phi$) and reflectance ($|r|$) of the end facets of an untapered coaxial waveguide with 75 nm wide dielectric channel and outer radius of 175 nm at a wavelength $\lambda_0 = 800$ nm derived from finite difference time domain simulations. (a) $\Delta\phi$ and $|r|$ are plotted as a function of the surrounding dielectric index for waveguides with fixed dielectric channel index, $n_{in} = 1.5$. The dotted blue line gives the result obtained from Fresnel equations using the (single) mode index of the coaxial cavity. (b) Plot of $\Delta\phi$ and $|r|$ as a function of the refractive index of the dielectric channel of the coaxial waveguide, while the surrounding dielectric index is kept fixed, $n_{out} = 1.0$.

1.0 to 3.5. The data demonstrate that the reflection phase depends strongly on the surrounding index and can be tuned to any value between 0 and π. It is worthwhile to note that the observed trend qualitatively agrees with the trend given by a calculation using the Fresnel equations (blue dotted line) using the mode index of the cavity. Quantitatively however, the trend observed for coaxes is very different, and may only be obtained analytically if we consider mode overlap between waveguide modes, surface waves, and free-space modes. Interestingly, a change in the refractive index of the surrounding medium hardly affects the end facet reflectance of ~70%.

Figure 7b shows the influence of a change in the dielectric channel index on the reflection coefficients of the coaxial waveguide when the refractive index of the surrounding medium is fixed at $n_{out} = 1.0$. As the refractive index of the dielectric in the coaxial waveguide is increased from 1.0 to 2.5, we find that the end fact reflectance increases from ~55% to ~85%, while the phase shift on reflection off the cavity ends remains at a value of ~0.1π. In general, we find that an increase of the effective mode index of the waveguide either by a change in the refractive index of the dielectric or by a change in the geometry leads to an improved cavity end reflectance.

Figure 7 demonstrates that the reflection phase and reflectance of the cavity end facets can be independently tuned. This opens the way to realization of plasmonic cavities

with ultrasmall mode volumes, where the reflection phase can effectively cancel the phase accumulated during propagation in the coaxial waveguide,[24] enabling cavities with a length considerably shorter than $\lambda/2$. The quality factor of the cavity is mainly dependent on the reflectance of the cavity mirrors, which, as we have shown, can be improved by increasing the effective index inside the coax, for instance by reducing the dielectric channel width in the cavity. Counterintuitively, a reduction in channel width may thus give rise to a smaller mode volume as well as a greater quality factor.

In conclusion, we have shown that the plasmon dispersion in coaxial waveguides with subwavelength dimensions can be determined from single-cavity transmission measurements. Our dispersion data agree well with an analytical model for dispersion in coaxial waveguides of infinite length and demonstrate the large degree of tunability by varying the coaxial cavity dimensions and dielectric medium. A plasmon phase shift up to π occurs upon reflection off the cavity ends and strongly affects the cavity resonance. The phase shift depends greatly on the waveguide geometry and dielectric medium inside and outside the cavity, providing further tunability of the coaxial cavity resonances and enabling cavities with ultrasmall mode volumes. The fundamental insights obtained in this paper are important in further studies of nanoscale waveguiding, field enhancement, and imaging with coaxial cavities, as well as their use in negative-index metamaterials.

References

(1) Mühlschlegel, P.; Eisler, H. J.; Martin, O. J. F.; Hecht, B.; Pohl, D. W. *Science* **2005**, *308*, 1607–1609.
(2) de Waele, R.; Koenderink, A. F.; Polman, A. *Nano Lett.* **2007**, *7*, 2004–2008.
(3) Verhagen, E.; Polman, A.; Kuipers, L. *Opt. Express* **2008**, *16*, 45–57.
(4) Nie, S.; Emery, S. R. *Science* **1997**, *275*, 1102–1106.
(5) Hubert, C.; Rumyantseva, A.; Lerondel, G.; Grand, J.; Kostcheev, S.; Billot, L.; Vial, A.; Bachelot, R.; Royer, P.; Chang, S. H.; Gray, S. K.; Wiederrecht, G. P.; Schatz, G. C. *Nano Lett.* **2005**, *5*, 615–619.
(6) Koenderink, A. F.; Hernández, J. V.; Robicheaux, F.; Noordam, L. D.; Polman, A. *Nano Lett.* **2007**, *7*, 745–749.
(7) Miyazaki, H. T.; Kurokawa, Y. *Phys. Rev. Lett.* **2006**, *96*, 097401.
(8) Pendry, J. B. *Phys. Rev. Lett.* **2000**, *85*, 3966–3969.
(9) Fang, N.; Lee, H.; Sun, C.; Zhang, X. *Science* **2005**, *308*, 534–537.
(10) Pendry, J. B.; Schurig, D.; Smith, D. R. *Science* **2006**, *312*, 1780–1782.
(11) Alù, A.; Engheta, N. *Phys. Rev. Lett.* **2008**, *100*, 113901.
(12) Fan, W.; Zhang, S.; Minhas, B.; Malloy, K. J.; Brueck, S. R. J. *Phys. Rev. Lett.* **2005**, *94*, 033902.
(13) Salvi, J.; Roussey, M.; Baida, F. I.; Bernal, M. P.; Mussot, A.; Sylvestre, T.; Maillotte, H.; Van Labeke, D.; Perentes, A.; Utke, I.; Sandu, C.; Hoffmann, P.; Dwir, B. *Opt. Lett.* **2005**, *30*, 1611–1613.
(14) Orbons, S. M.; Roberts, A.; Jamieson, D. N.; Haftel, M. I.; Schlockermann, C.; Freeman, D.; Luther-Davies, B. *Appl. Phys. Lett.* **2007**, *90*, 251107.
(15) Baida, F. I.; Belkhir, A.; Van Labeke, D.; Lamrous, O. *Phys. Rev. B* **2006**, *74*, 205419.
(16) Haftel, M. I.; Schlockermann, C.; Blumberg, G. *Phys. Rev. B* **2006**, *74*, 235405.
(17) Haftel, M. I.; Schlockermann, C.; Blumberg, G. *Appl. Phys. Lett.* **2006**, *88*, 193104.
(18) Van Labeke, D.; Gerard, D.; Guizal, B.; Baida, F. I.; Li, L. *Opt. Express* **2006**, *14*, 11945–11951.
(19) Stratton, J. A. *Electromagnetic theory*, 1st ed.; McGraw-Hill Book Company: New York and London, 1941.
(20) Marcuse, D. *Light transmission optics*; Van Nostrand Reinhold: New York, 1972.
(21) Novotny, L.; Hafner, C. *Phys. Rev. E* **1994**, *50*, 4094–4106.
(22) Schider, G.; Krenn, J.; Hohenau, A.; Ditlbacher, H.; Leitner, A.; Aussenegg, F.; Schaich, W.; Puscasu, I.; Monacelli, B.; Boreman, G. *Phys. Rev. B* **2003**, *68*, 155427.
(23) Ditlbacher, H.; Hohenau, A.; Wagner, D.; Kreibig, U.; Rogers, M.; Hofer, F.; Aussenegg, F. R.; Krenn, J. R. *Phys. Rev. Lett.* **2005**, *95*, 257403.
(24) Feigenbaum, E.; Orenstein, M. *Phys. Rev. Lett.* **2008**, *101*, 163902.

NL900597Z